Nanoscale

Accepted Manuscript

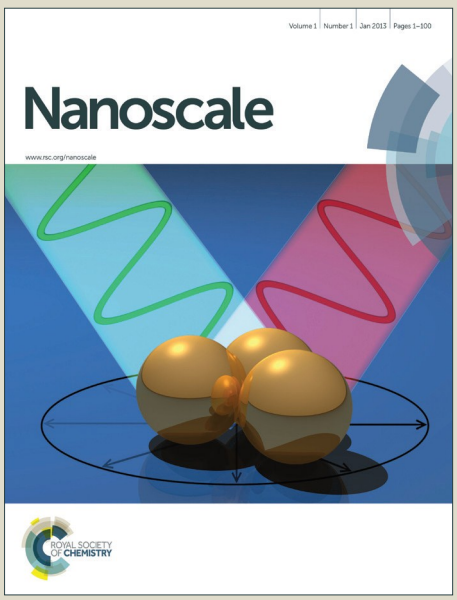

ROYAL SOCIETY OF CHEMISTRY

www.rsc.org/nanoscale

Journal Name

RSCPublishing

ARTICLE

Lanthanides post-functionalized nanocrystalline metal-organic frameworks for tunable white-light emission and orthogonal multi-Readout thermometry

*Cite this: DOI: 10.1039/x0xx00000x

Received 00th January 2012,
Accepted 00th January 2012

DOI: 10.1039/x0xx00000x

www.rsc.org/

You Zhou, Bing Yan*

We demonstrate tunable white-light emission and multi-readout thermometry in two respective nanocrystalline luminescent metal-organic frameworks (MOFs), which are prepared via postsynthetic functionalization with lanthanide cations of a robust UiO type MOF bearing the 2,2'-bipyridyl moiety (UiO-67-bpydc, **1**).The white-light emitting framework Eu^{3+}**@1** can be conveniently applied as a thin film onto a commercial UV-LED chip for practical white lighting applications. The multi-readout orthogonal thermometry is illustrated in connection to emission intensity ratio as well as decay time and luminescence color of Eu^{3+}/Tb^{3+}**@1** nanocrystals. This work highlights the opportunity in designing white-light emitters and nanothermometers based on lanthanides functionalized MOFs.

Introduction

Luminescent metal-organic frameworks (MOFs) featuring permanent porosity and intense emission have emerged as very attractive functional hybrid materials in the past decade.[1-4] Compared with the traditional inorganic and organic luminescent materials, the fluorescence of MOFs is more diverse because of that both the metal centers and organic moieties within porous MOFs can provide the platforms to generate luminescence. In addition, ligand-metal charge transfer and some guest species within MOFs offer additional luminescence. Such fascinating characteristics enable us to fabricate luminescent MOF materials with systematically varied emissions. Of them, white-light emitting MOFs are of particular interest owing to their potential applications in displays and solid-state lighting.[5-14] The white-light emission in MOFs is commonly generated from two pathways, including i) monochromatic luminescence center that emit broad-band white-light emission,[7,9,10]and ii) dichromatic luminescence centers that offer a synergetic contribution to come up with white-light emission.[5,13-16] The dual emission pathway generally gives rise to finer color-rendering properties and higher luminescent quantum yields, thus gaining more popularity. To date, a very small number of white-light emitting MOFs resulting from a dual emission approach have been achieved through lanthanides doping,[13, 15-17] and iridium-complex[6] or dye[18] encapsulation. Furthermore, the practical application in white-light-emitting-diode of these white-light emitting MOFs has rarely been demonstrated.

In addition to the promising applications in displays and light-emitting devices, luminescent MOFs are well suited for developing fluorescent probes owing to their tunable intriguing structures and permanent porosity. Sensing for metal cations,[19-21] anions,[22,23] small molecules,[24-26] and vapors[27,28] has been well demonstrated in luminescent MOFs. Recently, there has been an escalating interest in developing temperature sensors based on luminescent MOFs. Since Cui et al. pioneered a mixed lanthanides MOF approach to fabricate ratiometric luminescent thermometers,[29] a variety of MOF thermometers has been achieved.[30-35] Compared with the thermal probes relied on the conventional methods, such luminescence-based thermometers gain more popularity due to their noninvasive, accuracy and their ability to work even in strong electromagnetic fields and fast-moving objects. Nevertheless, all these MOF thermometers are simply relied on a single readout system (emission intensity ratio). To maximize the available information and enhance the

power of temperature detection, luminescence thermometers with orthogonal multi-readout are desired. Moreover, the existing MOF thermometers are bulk crystals[29-31,33,34] or highly aggregated nanoparticles,[32,35] which severely hinder their applications in nanotechnology and biomedicine.

In this contribution we report two luminescent nanocrystalline MOFs for tunable white-light emitter and orthogonal multi-readout nanothermometer, respectively. These two luminescent nanocrystalline MOFs are prepared via postsynthetic functionalization with lanthanide cations of a robust UiO type MOF bearing the 2,2'-bipyridyl moiety (UiO-67-bpydc, **1**).The white-light emitter Eu^{3+}@**1** can be conveniently applied as a thin film onto a commercial UV-LED chip for practical white lighting applications. The orthogonal multi-readout thermometry is demonstrated in connection to emission intensity ratio as well as decay time and luminescence color of Eu^{3+}/Tb^{3+}@**1** nanocrystals.

Experimental Section

Synthesis of UiO-67-bpydc (1). MOF 1 was prepared from the modified procedure from the literature.[36] Ligand 2,2'-bipyridine-5,5'-dicarboxylate acid (H_2bpydc, 0.248 g, 1 mmol), $ZrCl_4$ (0.233 g, 1 mmol), glacial acetic acid (2.0 g, 33.33 mmol) were mixed in 60 ml DMF. Glacial acetic acid was added to provide better crystallinity of the product. After 30 minutes of stirring at ambient conditions, the mixture was transferred into a 100 ml Teflon-lined stainless steel container and then heated at 393 K for 24 h. The resulting white powder was separated from the mixed dispersion by centrifugation and washed with DMF and methanol. To remove the organic species encapsulated within the pores of the open framework, the product was washed with methanol via Soxhlet extraction for 24 h, followed by drying at 80 °C under vacuum.

Synthesis of Eu^{3+}@1. Compound **1** (50 mg, 0.134 mmol), $EuCl_3{\cdot}6H_2O$ (49 mg, 0.134 mmol), and methanol (10 ml) were added to a 20 ml Pyrex tube and heated at 333 K for 24 h. The solid was then filtered off and soaked in 15 ml methanol. After 24 h, the supernatant was decanted and replaced by fresh methanol. This procedure was repeated two times to guarantee that all excess $EuCl_3$ salt is removed. Finally, the product was collected by filtration and dried at 353 K under vacuum.

Synthesis of Tb^{3+}@1. Compound **1** (50 mg, 0.134 mmol), $TbCl_3{\cdot}6H_2O$ (50 mg, 0.134 mmol), and methanol (10 ml) were added to a 20 ml Pyrex tube and heated at 333 K for 24 h. The solid was then filtered off and soaked in 15 ml methanol. After 24 h, the supernatant was decanted and replaced by fresh methanol. This procedure was repeated two times to guarantee that all excess $TbCl_3$ salt is removed. Finally, the product was collected by filtration and dried at 353 K under vacuum.

Synthesis of Eu^{3+}/Tb^{3+}@1. Compound **1** (50 mg, 0.134 mmol), $EuCl_3{\cdot}6H_2O$ (0.245 mg, $6.7 \cdot 10^{-4}$mmol), $TbCl_3{\cdot}6H_2O$ (49.62 mg, 0.133 mmol), and methanol (10 ml) were added to a 20 ml Pyrex tube and heated at 333 K for 24 h. The solid was then filtered off and soaked in 15 ml methanol. After 24 h, the supernatant was decanted and replaced by fresh methanol. This procedure was repeated two times to guarantee that all excess $TbCl_3$ salt is removed. Finally, the product was collected by filtration and dried at 353 K under vacuum.

White LED fabrication and performance measurement. The white LED was achieved by coating a thin film of Eu^{3+}@**1** onto a commercially available 375 nm UV-LED chip through a simple and efficient dip coating procedure (similar to that reported by He and co-workers).[37] Specifically, nanocrystals of Eu^{3+}@**1** (about 10 mg) were dispersed in 1.0 mL methanol, followed by ultrasonic treatment until a significant portion of the methanol was evaporated and a homogeneous suspension was achieved. The final volume of the suspension is about 0.1 mL.A commercial 375 nm UV-LED chip was then dipped into the suspension and held therein for several seconds. Afterwards, UV-LED chip was taken out for the coating to dry in air. This dip coating process was repeated two times to further ensure that the coating on the LED chip is even and continuous.

The photoelectric properties of the fabricated devices were determined by an integrating sphere spectroradiometer system (LHS-1000, Everfine). The spectral power distributions of the LEDs were measured by a corrected spectrometer to calculate their values of CCT and CRI (ref. [38]). The luminous efficacy was measured as the ratio of luminous flux (lm) output to the input electrical power (W) of the LEDs.

Characterization. Powder X-ray diffraction patterns (PXRD) were recorded with a Bruker D8 diffractometer using CuKα radiation with 40 mA and 40 kV. Inductively coupled plasma-mass spectrometry (ICP-MS) data were obtained on an X-7 series inductively coupled plasma-mass spectrometer (Thermo Elemental, Cheshire, UK), ICP samples were prepared by digesting the dry samples of Ln^{3+}@**1** into concentrated HNO_3, followed by the dilution to 0.5% HNO_3 solution. Transmission electron microscopy (TEM) was carried out on a JEOL JEM-2100F electron microscope and operated at 200 kV. Thermogravimetric analysis (TGA) was measured using a Netzsch STA 449C system at a heating rate of 5 K min^{-1} under the nitrogen protection.

The photoluminescence spectra and luminescent decay times were examined by an Edinburgh FLS920 phosphorimeter. The absolute external luminescent quantum efficiency was determined employing an integrating sphere (150 mm diameter, $BaSO_4$ coating) from an Edinburgh FLS920 phosphorimeter. The spectra were corrected for variations in the output of the excitation

source and for variations in the detector response. The quantum yield can be defined as the integrated intensity of the luminescence signal divided by the integrated intensity of the absorption signal. The absorption intensity was calculated by subtracting the integrated intensity of the light source with the sample in the integrating sphere from the integrated intensity of the light source with a blank sample in the integrating sphere. The excitation wavelength of the measurements of the emission quantum yields was listed in Table 1. The estimated errors for quantum yields and luminescent lifetime are within 5%.

Table 1. Luminescent Lifetime (τ) and Absolute Quantum Yields (ϕ) of Ln^{3+}@**1** (Ln^{3+} = Eu^{3+}, Tb^{3+}, Eu^{3+}/Tb^{3+}).

Ln^{3+}	τ (ms)	Φ (%)	λ_{ex} (nm)
Eu^{3+}	0.261 [a]	14.34	344
Tb^{3+}	0.107 [b]	3.18	338
Eu^{3+}/Tb^{3+}	0.413 [a]/0.063 [b]	10.48	337

[a] For the $^5D_0 \rightarrow {}^7F_2$ transition of Eu^{3+}, λ_{em} = 613 nm. [b] The transition $^5D_4 \rightarrow {}^7F_5$ of Tb^{3+}, λ_{em} = 545 nm.

Results and Discussion

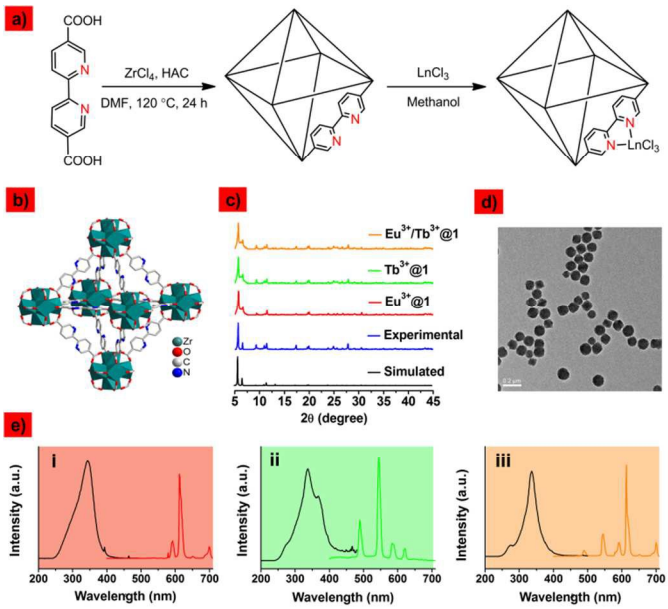

Figure 1. a) Schematic illustration of synthesis and postsynthetic Ln^{3+} functionalization of MOF **1**. b) X-ray crystal structure of **1**. The figure was drawn using structural data taken from ref. 39. c) PXRD patterns of that simulated from the CIF file [39] (black), pristine 1 (blue), and Ln^{3+}@**1** samples (red, green and orange for Eu^{3+}@**1**, Tb^{3+}@**1**, and Eu^{3+}/Tb^{3+}@**1** respectively). d) Typical TEM image of nanocrystals of **1**. The scale bar is 200 nm. e) Excitation and emission spectra of Eu^{3+}@**1** (i), Tb^{3+}@**1** (ii), and Eu^{3+}/Tb^{3+}@**1** (iii).

MOFUiO-67-bpydc (**1**) was synthesized by a solvothermal reaction of $ZrCl_4$ and 2,2'-bipyridine-5,5'-dicarboxylic acid (H_2bpydc) in the presence of DMF and glacial acetic acid (Figure 1a). The resulting white solid showed an identical powder X-ray diffraction pattern (PXRD) to that simulated from the single crystal structure (Figure 1b, 1c).[39] The three dimension framework with *fcu* topology of **1** is constructed by bridging the 2,2'-bipyridine-5,5'-dicarboxylate acid (bpydc) linkers with the 12-connected second building units (SBUs), which is formed by the assembly of six zirconium atoms with eight μ^3-O or μ^3-OH linked oxygen atoms and twelve carboxylate groups (Figure 1b).TEM study indicated that the product consists of monodisperse nanocrystals with a uniform size of ~100 nm (Figure 1d). It is noteworthy that the bipyridyl moieties were incorporated as free Lewis basic sites, thus allowing the encapsulation of lanthanide cations (Ln^{3+}) within MOF **1**.

The post-functionalization of **1** was performed by immersing the nanocrystals of **1** in methanol solution of chlorine salts of Eu^{3+}, Tb^{3+}, and Eu^{3+}/Tb^{3+} (0.995/0.005), which afford Eu^{3+}@**1**, Tb^{3+}@**1** , and Eu^{3+}/Tb^{3+}@**1**. The Ln^{3+} loading levels of the Ln^{3+}@**1** samples were quantified by inductively coupled plasma-mass spectrometry (ICP-MS) analyses, as demonstrated in Table S1.Ln^{3+}@**1** products exhibit broadening diffraction peaks in comparison with that of the parented framework **1** (Figure 1c). However, the PXRD patterns of the isolated **1** and Ln^{3+}@1 products are considerably identical, in both the position and in relative intensity of the main diffraction peaks, indicating that the crystal structure of framework **1** is remained in Ln^{3+}@1 samples. The morphology and size of the nanocrystals of **1** were also unchanged upon metalation with Ln^{3+} (Figure S1-S3). Thermogravimetric analysis shows that these Ln^{3+}@**1** products were thermally stable to 723 K (Figure S4), which is in reasonable agreement with that of the parented isolated framework **1**. It further confirmed the integrity of framework **1** is maintained afterLn^{3+} incorporation.

Under UV irradiation at room temperature, compound **1** exhibited a broad emission band ranging from 400 to 650 nm (Figure S5), which is resulted from the bpydc linkers. To verify this, we present solid-state excitation and emission spectra of the corresponding free ligand of H_2bpydc. As shown in Figure S6, the emission spectrum of H_2bpydc rather resembles that of**1** except a slight blue shifting of the wavelength, suggesting the luminescence of **1** could be regarded as metal-perturbed linker-centered emission. Figure 1e presents the photoluminescence studies of Eu^{3+}@**1**, Tb^{3+}@**1**,and Eu^{3+}/Tb^{3+}@**1**. The excitation spectra of the Ln^{3+}@**1** samples all display an intense and broad band with a maximum at around 340 nm due to the π–π* electron transition of bpydc linkers. Upon excitation at 340 nm, Eu^{3+}@**1** shows characteristic sharp emissions of Eu^{3+} centered at 579, 590, 616, 653, 701 nm which are originated from the $^5D_0 \rightarrow {}^7F_J$ (J = 0–4) transitions of Eu^{3+}, while Tb^{3+}@**1** exhibits emissions at 489, 544, 587, and 622 nm which are from the $^5D_4 \rightarrow {}^7F_J$ (J = 6, 5, 4, and 3) transitions of Tb^{3+}. These reveal that the Ln^{3+} emission can be sensitized by the bpydc linkers embedded in framework **1**. The energy transfer from bpydc ligands to Ln^{3+}cations is efficient, as confirmed by the diminished ligand emission in Ln^{3+}@1. As for Eu^{3+}/Tb^{3+}@**1**, the emission spectrum displays dual emissions of Eu^{3+} and Tb^{3+}. In addition, the

luminescence of Eu^{3+}/Tb^{3+}@**1** can be tuned by modifying the ratio of the incorporatedEu^{3+} and Tb^{3+} (Figure S7).The luminescence lifetime and quantum yields of the Ln^{3+}@**1** products were also determined (Table 1). These samples exhibit reasonable long luminescence lifetime and high quantum yields, implying that they can be utilized as excellent candidates for light-emitting devices and luminescent sensors.

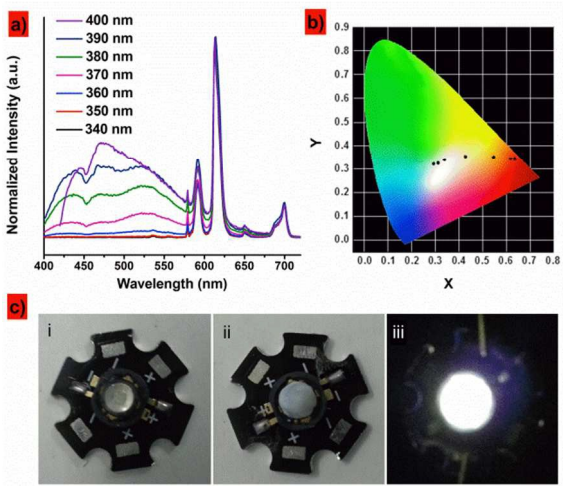

Figure 2. a) Emission spectra of Eu^{3+}@**1** when excited by the wavelength at 340-400 nm. Spectra were normalized to the $^5D_0 \rightarrow {}^7F_2$ transition of Eu^{3+}. b) CIE chromaticity diagram showing the luminescent color of Eu^{3+}@**1** under various excitation wavelengths. c) Photographs of a UV (375 nm) InGaAsN LED chip (i), the same LED coated with a thin layer of nanocrystals of Eu^{3+}@**1** (ii), and the coated LED turned on and illuminating bright white light (iii).

As both framework **1** and the incorporated Ln^{3+} cations contribute to the compound's luminescence, we reasoned that a fine tuning of emission color can be achieved by modulating the excitation wavelength. Figure 2a depicts the emission spectra of Eu^{3+}@**1**with excitation wavelength from 340 to 400 nm. The excitations at different wavelengths give rise to different emission intensity relativity of these two kinds of luminescence (Eu^{3+} emission and the ligand-centered emission), thus leading to a shift of the chromaticity coordinate in the chromaticity diagram. As shown in Figure 2b, the calculated chromaticity from the emission spectra of Eu^{3+}@**1** moves from the red region to the white region as the excitation wavelength varying from 340 to 400 nm. Notably, the coordinates are (0.4267, 0.3557), (0.3372, 0.3419), and (0.3102, 0.3265) when the Eu^{3+}@**1**sample is excited at respective 370, 380, and 390 nm, which closely approach the optimum white-light chromaticity coordinates (0.33, 0.33) established by the Commission Internationalede l'Eclairage (CIE). It highlights the opportunity of Eu^{3+}@**1** to develop as white-light emitting devices.

Figure 2c demonstrates the white LED fabricated by combining Eu^{3+}@**1**nanophosphors with a UV LED chip. A thin layer of Eu^{3+}@**1** prepared from a methanol solution was coated onto a commercially available UV-LED chip through a simple and efficient dip coating procedure. The performance of the white LED thus prepared is stable for months in air. Upon illumination, it generated bright white light. The electroluminescence spectrum of the white LED under a drive current of 150 mA presents a broad emission band in range of 400-550 nm band and several sharp lines ranging from 570 to 710 nm, which corresponds to the ligand-centered emission and Eu^{3+} emission, respectively (Figure S8). The CIE and CCT values are respective (0.3481, 0.3292) and 4914 K, as shown in Figure S9. The CRI is determined as 75, which is smaller than the counterpart using a MOF phosphor[6] but still exceeds the value of commercial white LED using a single YAG:Ce^{3+} phosphor (R_a< 70).[40] The luminous efficiency of the fabricated LED is 32 lm W^{-1}. This value is much higher that of the common incandescent lamps (< 18 lm W^{-1}), though it is smaller than the LEDs prepared by combining blue chips and multicomponent inorganic phosphors.[41,42]

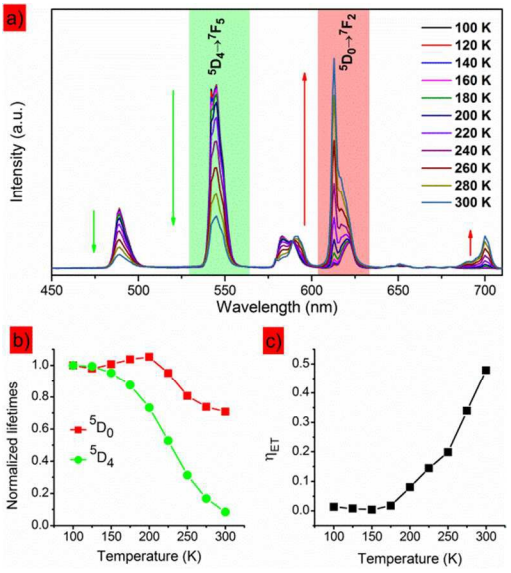

Figure 3.a) Temperature-dependent emission spectra (λ_{ex} = 340 nm) of Eu^{3+}/Tb^{3+}@**1** nanocrystals. Spectra were normalized to the total integrated intensity. b) The $^5D_4$ and $^5D_0$ lifetime of Eu^{3+}/Tb^{3+}@**1** as a function of temperature. (c) Temperature dependence of Tb^{3+} to Eu^{3+} energy transfer efficiency (η_{ET}) in Eu^{3+}/Tb^{3+}@**1**.

Toexamine the feasibility of theEu^{3+}/Tb^{3+}@**1**nanocrystals for ratiometric thermometry, we determined the thermometric response of Eu^{3+}/Tb^{3+}@**1** from T = 100-300 K. As shown in Figure 3a, Eu^{3+}/Tb^{3+}@**1**displays an exactly contrary thermal dependence with respect to the emissions of Tb^{3+} and Eu^{3+}. As the temperature rises, the Tb^{3+} emission intensity decreases sharply, while the Eu^{3+} emission significantly enhances. The similar unique luminescent behavior has been observed in the recently reported luminescent thermometers based on Eu/Tb mixed MOFs, and of which the different thermal dependences of Eu^{3+} and Tb^{3+} emissions were attributed to the Tb^{3+} to Eu^{3+} energy transfer mechanism.[29-32,35] To verify

the applicability of this mechanism to Eu^{3+}/Tb^{3+}@**1**, the temperature-dependent decay times of Eu^{3+}/Tb^{3+}@**1** ($^5D_0 \rightarrow {}^7F_2$ and $^5D_4 \rightarrow {}^7F_5$) were performed. The decay time of $^5D_4$ declines dramatically with temperature rising from 100to 300K, while the lifetime of $^5D_0$ increases from 0.666 ms at 100 K to 0.701 ms at 200 K (Figure 3b). In addition, the $^5D_0$ decay curves under excitation via the excited-ligand levels exhibit a rising part in the range of 0.1 to 0.3 ms (Figures S10). These phenomena indicate the occurrence of Tb^{3+} to Eu^{3+} energy transfer in Eu^{3+}/Tb^{3+}@**1**. Further evidence for the Tb^{3+} to Eu^{3+} energy transfer process is forthcoming from that Eu^{3+}/Tb^{3+}@**1**nanoparticles always exhibit shorter $^5D_4$ lifetime than Tb^{3+}@**1** but longer $^5D_0$ lifetime than Eu^{3+}@**1** at the same temperature (Table S2). The Tb^{3+} to Eu^{3+} energy transfer efficiency (η_{ET}) can be determined by equation (1)[43,44]

$$(\eta_{ET}) = 1 - \tau/\tau_o \qquad (1)$$

Here, τ and τ_o are $^5D_4$ donor lifetime in the presence and absence of the Eu^{3+} acceptors, respectively. As shown in Figure 3c, the values of η_{ET} are essentially unchanged at the low temperature range of 100-175 K, above which a rapid increase of η_{ET} is observed. It suggests that Tb^{3+} to Eu^{3+} energy transfer process can be rationalized by thermally driven phonon-assisted Förster transfer mechanism.

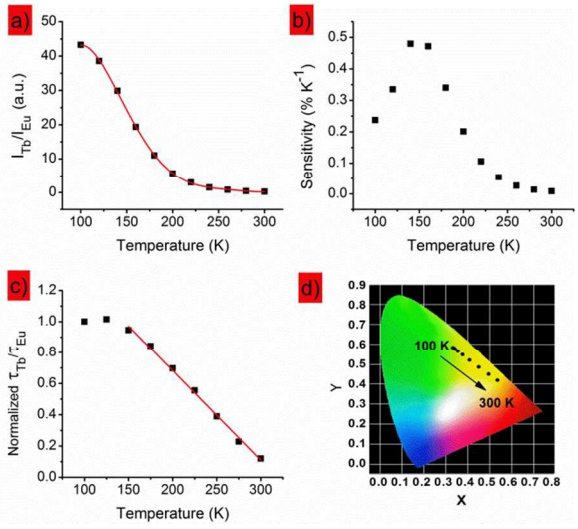

Figure 4. Eu^{3+}/Tb^{3+}@**1** nanocrystals show multi-readout orthogonal detection of temperature. a) Thermometric response curve plotting $I_{Tb(^5D_4 \rightarrow {}^7F_5)}/I_{Eu(^5D_0 \rightarrow {}^7F_2)}$ vs temperature. b) The relative thermometric sensitivity determined from a. c) $\tau_{Tb(^5D_4 \rightarrow {}^7F_5)}/\tau_{Eu(^5D_0 \rightarrow {}^7F_2)}$ as a function of temperature. d) Thermal dependence of the luminescence color.

The thermal sensitive luminescence properties enable Eu^{3+}/Tb^{3+}@**1** to serve as a nanoplatform for temperature sensing. Luminescent thermometers commonly rely on a single readout system, such as emission intensity,[45,46] luminescence decay time,[47,48] and emission intensity ratio.[49-55] Here we present a multi-readout orthogonal detection scheme based on Eu^{3+}/Tb^{3+}@**1** nanocrystals, which is demonstrated in connection to emission intensity ratio as well as decay time and luminescence color of Eu^{3+}/Tb^{3+}@**1** nanocrystals (Figure 4). For intensity ratio-based temperature readout, the ratiometric parameter is defined as the ratio of the intensity of $^5D_4 \rightarrow {}^7F_5$ of Tb^{3+} (544 nm) and $^5D_0 \rightarrow {}^7F_2$ of Eu^{3+} (616 nm). Figure 4a illustrates the thermometric response curve measured for Eu^{3+}/Tb^{3+}@**1**nanocrystals, plotting the emission intensity ratio as a function of temperature. These data show a best thermometric sensitivity of 47.98% K^{-1}at 140 K (Figure 4b), which is the largest one measured so far for the thermometers using the same intensity ratio technique. When setting a minimum sensitivity value of 2.5 % K^{-1} as quality limit, an optimal operation range of 100-260 K can be achieved. Although this intensity ratio-based method is not very reliable for temperature report in the range of 100-140 K because of the significantly weak emission of Eu^{3+}, it offers ultrahigh sensitive thermal detection at elevated temperature.

For the readout relied on decay times, similarly, the normalized luminescence lifetime ratio of $^5D_4$ and $^5D_0$ (τ_{Tb}/τ_{Eu}) of Eu^{3+}/Tb^{3+}@**1** is defined as thermometric parameter. Figure 4c plots the dependence of I_{Tb}/I_{Eu} on temperature, which reveals a good linear relationship between normalized τ_{Tb}/τ_{Eu} and temperature within the range of 150 to 300 K with a slope of 0.57% K^{-1}. Compared to the luminescence–intensity plot, the decay-time plot presents a smaller sensitivity towards temperature. Besides, Eu^{3+}/Tb^{3+}@**1** nanocrystals can also be developed as a colorimetric thermometer. As depicted in Figure 4d, the chromaticity diagram coordinates transformed from the temperature-dependent emission spectra (Figure 3a) shift from green to orange. It indicates the variation of ambient temperature can be estimated by observing the luminescent color of Eu^{3+}/Tb^{3+}@**1** using naked eyes or a CCD camera. The ability of in situ visualizing the temperature change instantly and straightforwardly makes this colorimetric method a useful avenue for thermometry, though the sensitivity and reliability of the colorimetric method can't be comparable with that of the method based on intensity ratio.

The multi-readout orthogonal thermometry based on three different photoluminescence characteristics (intensity ratio, decay time, and emission color) is capable of maximizing the available information and enhancing the power of temperature detection. Therefore, it is reasonable to expect that this multi-readout orthogonal detection scheme will be more reliable and powerful in temperature sensing.

Conclusions

In summary, we have developed two nanocrystalline lanthanides functionalized MOFs, Eu^{3+}@**1** and Eu^{3+}/Tb^{3+}@**1**, as tunable white-light emitter and multi-readout nanothermomter, respectively. By coating a thin layer of Eu^{3+}@**1** nanocrystals onto a commercial 375 nm UV

chip, we have achieved a high-performance white LED with a CIE, CRI, CCT values of (0.3481, 0.3292), 75, and 4914 K. The multi-readout orthogonal detection scheme is demonstrated in connection to emission intensity ratio as well as decay time and luminescence color of Eu^{3+}/Tb^{3+}@**1.** In particular, the ratiometric thermometry based on intensity ratio of Tb^{3+} ($^5D_4 \rightarrow {}^7F_5$) and Eu^{3+} ($^5D_0 \rightarrow {}^7F_2$) shows a best thermometric sensitivity of 47.98% K^{-1} (Figure 4b), which is the largest one measured so far for the thermometers using the same intensity ratio technique. This work highlights the opportunity in designing excellent white-light emitters and highly sensitive nanothermometers based on lanthanides functionalized MOFs.

Acknowledgements

This work was supported by the National Natural Science Foundation of China (91122003), Developing Science Funds of Tongji University and Science & Technology Commission of Shanghai Municipality (14DZ2261100).

Notes and References

[a] Department of Chemistry, and Shanghai Key Lab of Chemical Assessment and Substainability, Tongji University, Siping Road 1239, Shanghai 200092, China. E-mail: byan@tongji.edu.cn; Fax: +86-21-65982287;
Tel: +86-21-65984663

†Electronic Supplementary Information (ESI) available: [details of any supplementary information available should be included here]. See DOI: 10.1039/b000000x/

1 Z. C. Hu, B. J. Deibert and J. Li, *Chem. Soc.Rev.*, 2014, **43**,5815-5840.
2 Y. J. Cui, B. L. Chen and G. D. Qian, *Coord. Chem. Rev.*, 2014, **273**, 76-86.
3 Y. J. Cui, Y. F. Yue, G. D. Qian and B. L. Chen, *Chem. Rev.*, 2012, **112**, 1126-1162.
4 J. Rocha, L. D. Carlos, F. A. A. Paz and D. Ananias, *Chem. Soc.Rev.*, 2011, **40**, 926-940.
5 Y. Liu, M. Pan, Q. Y. Yang, L. Fu, K. Li, S. C. Wei and C. Y. Su, *Chem. Mater.*, 2012, **24**, 1954-1960.
6 C. Y. Sun, X. L. Wang, X. Zhang, C. Qin, P. Li, Z. M. Su, D. X. Zhu, G. G. Shan, K. Z. Shao, H. Wu and J. Li, *Nat.Commun.*, 2013, **4**, 2717.
7 D. F. Sava, L. E. S. Rohwer, M. A. Rodriguez and T. M. Nenoff, *J. Am. Chem. Soc.*, 2012, **134**, 3983-3986.
8 D. F. Sava, L. E. S. Rohwer, M. A. Rodriguez and T. M. Nenoff, *Chem. Mater.*, 2014, **26**, 2943-2951
9 M. S. Wang, S. P. Guo, Y. Li, L. Z. Cai, J. P. Zou, G. Xu, W. W. Zhou, F. K. Zheng and G. C. Guo, *J. Am. Chem. Soc.*, 2009, **131**, 13572-13573.
10 Q. Y. Yang, K. Wu, J. J. Jiang, C. W. Hsu, M. Pan, J. M. Lehn and C. Y. Su, *Chem.Commun.*, 2014, **50**, 7702-7704.
11 F. Luo, M. S. Wang, M. B. Luo, G. M. Sun, Y. M. Song, P. X. Li and G. C. Guo, *Chem.Commun.*, 2012, **48**, 5989-5991.
12 S. Dang, J. H. Zhang and Z. M. Sun, *J. Mater. Chem.*, 2012, **22**, 8868-8873.
13 Y. Zhou and B. Yan, *Inorg. Chem.*, 2014, **53**, 3456-3463.
14 Y. Lu and B. Yan, *Chem. Commun.* 2014, **50**, 15443-15446.
15 S. M. Li, X. J. Zheng, D. Q. Yuan, A. Ablet and L. P. Jin, *Inorg. Chem.* 2012, **51**, 1201-1203.
16 Q. Tang, S. X. Liu, Y. W. Liu, D. F. He, J. Miao, X. Q. Wang, Y. J. Ji and Z. P. Zheng, *Inorg. Chem.*, 2014, **53**, 289-293.
17 J. N. Hao and B. Yan, *J. Mater. Chem. C*, 2014, **2**, 6758-6764.
18 M. L. Ma, J. H. Qin, C. Ji, H. Xu, R. Wang, B. J. Li, S. Q. Zang, H. W. Hou and S. R. Batten, *J. Mater. Chem. C*, 2014, **2**, 1085-1093.
19 Y. Zhou, H. H. Chen and B. Yan, *J. Mater. Chem. A*, 2014, **2**, 13691-13697.
20 B. L. Chen, L. B. Wang, Y. Q. Xiao, F. R. Fronczek, M. Xue, Y. J. Cui and G. D. Qian, *Angew. Chem., Int. Edit.*, 2009, **48**, 500-503.
21 Y. Lu, B. Yan and J. L. Liu, *Chem.Commun.*, 2014, **50**, 9969-9972.
22 B. L. Chen, L. B. Wang, F. Zapata, G. D. Qian and E. B. Lobkovsky, *J. Am. Chem. Soc.*, 2008, **130**, 6718-6719.
23 Y. Q. Chen, G. R. Li, Z. Chang, Y. K. Qu, Y. H. Zhang and X. H. Bu, *Chem. Sci.*, 2013, **4**, 3678-3682.
24 H. L. Jiang, Y. Tatsu, Z. H. Lu and Q. Xu, *J. Am. Chem. Soc.*, 2010, **132**, 5586-5587.
25 B. L. Chen, Y. Yang, F. Zapata, G. N. Lin, G. D. Qian and E. B. Lobkovsky, *Adv. Mater.*, 2007, **19**, 1693-1696.
26 W. J. Rieter, K. M. L. Taylor and W. B. Lin, *J. Am. Chem. Soc.*, 2007, **129**, 9852-9853.
27 J. L. Chen, F. Y. Yi, H. Yu, S. H. Jiao, G. S. Pang and Z. M. Sun, *Chem.Commun.*, 2014, **50**, 10506-10509.
28 G. Lu, O. K. Farha, L. E. Kreno, P. M. Schoenecker, K. S. Walton, R. P. Van Duyne and J. T. Hupp, *Adv. Mater.* 2011, **23**, 4449-4452.
29 Y. J. Cui, H. Xu, Y. F. Yue, Z. Y. Guo, J. C. Yu, Z. X. Chen, J. K. Gao, Y. Yang, G. D. Qian and B. L. Chen, *J. Am. Chem. Soc.*, 2012, **134**, 3979-3982.
30 X. T. Rao, T. Song, J. K. Gao, Y. J. Cui, Y. Yang, C. D. Wu, B. L. Chen and G. D. Qian, *J. Am. Chem. Soc.*, 2013, **135**, 15559-15564.
31 Y. J. Cui, W. F. Zou, R. J. Song, J. C. Yu, W. Q. Zhang, Y. Yang and G. D. Qian, *Chem.Commun.*, 2014, **50**, 719-721.
32 A. Cadiau, C. D. S. Brites, P. M. F. J. Costa, R. A. S. Ferreira, J. Rocha and L. D. Carlos, *AcsNano*, 2013, **7**, 7213-7218.
33 K. Miyata, Y. Konno, T. Nakanishi, A. Kobayashi, M. Kato, K. Fushimi and Y. Hasegawa, *Angew. Chem.,Int, Edit.*, 2013, **52**, 6413-6416.
34 R. F. D'Vries, S. Alvarez-Garcia, N. Snejko, L. E. Bausa, E. Gutierrez-Puebla, A. de Andres and M. A. Monge, *J. Mater. Chem. C*, 2013, **1**, 6316-6324.
35 Y. Zhou, B. Yan and F. Lei, *Chem. Commun.*, 2014, **50**, 15235-15238.
36 H. H. Fei and S. M. Cohen, *Chem.Commun.*, 2014, **50**, 4810-4812.
37 J. He, M. Zeller, A. D. Hunter and Z. T. Xu, *J. Am. Chem. Soc.*, 2012, **134**, 1553-1559.
38 Y. Ohno, *Proc.SPIE* 2004, **5530**, 88-98.
39 L. J. Li, S. F. Tang, C. Wang, X. X. Lv, M. Jiang, H. Z. Wu and X. B. Zhao, *Chem.Commun.*, 2014, **50**, 2304-2307.
40 A. Birkel, K. A. Denault, N. C. George, C. E. Doll, B. Hery, A. A. Mikhailovsky, C. S. Birkel, B. C. Hong and R. Seshadri, *Chem. Mater.*, 2012, **24**, 1198-1204.

41 X. B. Wang, X. S. Yan, W. W. Li, and K. Sun, *Adv. Mater.,* 2012, **24**, 2742-2747.
42 H.M. Zhu, C. C. Lin, W. Q. Luo, A. T. Shu, Z. G. Liu, Y. H. Liu, J. T. Kong, E. Ma, Y. G. Ca01, R. S. Liu, and X. Y. Chen, *Nat. Commun.,* **2014**, 5, 4312.
43 M. O. Rodrigues, J. D. L. Dutra, L. A. O. Nunes, G. F. de Sa, W. M. de Azevedo, P. Silva, F. A. A. Paz, R. O. Freire and S. A. Junior, *J. Phys. Chem. C*, 2012, **116**, 19951-19957.
44 C. Piguet, J. C. G. Buzli, G. Bernardinelli, G. Hopfgartner, A. F. Williams, *J. Am. Chem. Soc.* 1993, **115**, 8197-8206.
45 H. S. Peng, M. I. J. Stich, J. B. Yu, L. N. Sun, L. H. Fischer and O. S. Wolfbeis, *Adv. Mater.*, 2010, **22**, 716-719.
46 A. P. Herrera, M. Rodriguez, M. Torres-Lugo and C. Rinaldi, *J. Mater. Chem.*, 2008, **18**, 855-858.
47 K. Okabe, N. Inada, C. Gota, Y. Harada, T. Funatsu and S. Uchiyama, *Nat. Commun.*, 2012, **3**, 705.
48 J. M. Yang, H. Yang and L. W. Lin, *AcsNano*, 2011, **5**, 5067-5071.
49 E. J. McLaurin, L. R. Bradshaw and D. R. Gamelin, *Chem. Mater.*, 2013, **25**, 1283-1292.
50 C. D. S. Brites, P. P. Lima, N. J. O. Silva, A. Millan, V. S. Amaral, F. Palacio and L. D. Carlos, *Adv. Mater.*, 2010, **22**, 4499-4504.
51 Y. Takei, S. Arai, A. Murata, M. Takabayashi, K. Oyama, S. Ishiwata, S. Takeoka and M. Suzuki, *AcsNano*, 2014, **8**, 198-206.
52 E. J. McLaurin, V. A. Vlaskin and D. R. Gamelin, *J. Am. Chem. Soc.*, 2011, **133**, 14978-14980.
53 F. M. Ye, C. F. Wu, Y. H. Jin, Y. H. Chan, X. J. Zhang and D. T. Chiu, *J. Am. Chem. Soc.*, 2011, **133**, 8146-8149.
54 A. E. Albers, E. M. Chan, P. M. McBride, C. M. Ajo-Franklin, B. E. Cohen and B. A. Helms, *J. Am. Chem. Soc.*, 2012, **134**, 9565-9568.
55 S. H. Zheng, W. B. Chen, D. Z. Tan, J, J. Zhou, Q. B. Guo, W. Jiang, C. Xu, X. F. Liu and J. R. Qiu, *Nanoscale,* 2014, **6**, 5675-5679